2.5. Histological analysis

Fluorescently labeled whole-mount tissues were analyzed by CLSM as described previously [8,22]. Each area of NKM 16-2-4$^+$ cells and whole FAE in PPs was quantitated using Scion Image software (Scion Corporation, Frederick, MA) based on the data obtained by CLSM (see Supplementary information).

2.6. Quantitative real-time RT-PCR for Fut1 and Fut2 transcripts

The levels of the *Fut1* and *Fut2* transcripts were quantitated by real-time RT-PCR in the cDNA samples from the sorted cells with reference to the level of hypoxanthine guanine phosphoribosyl transferase (*Hprt*) transcripts (see Supplementary information).

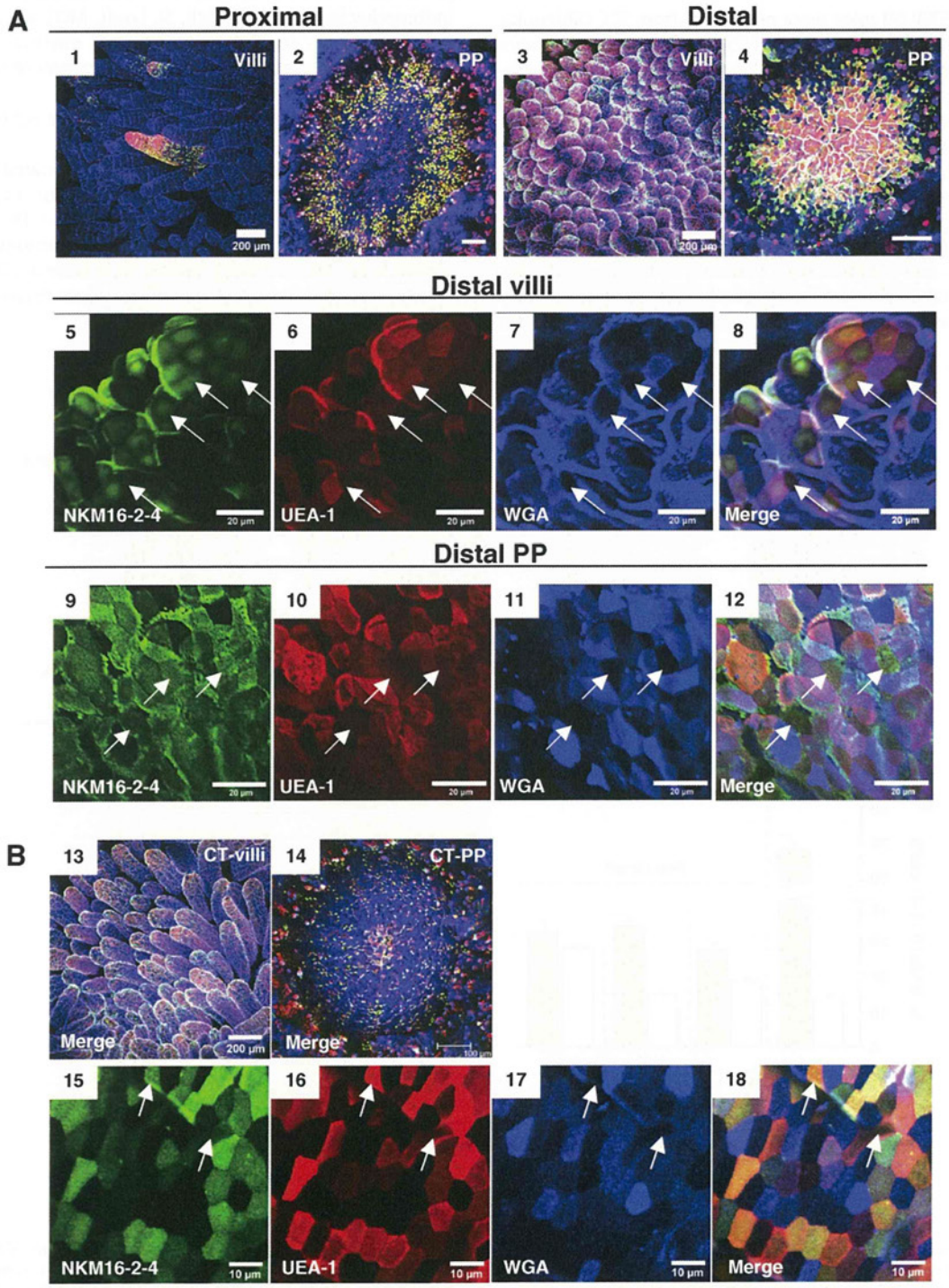

Fig. 2. CLSM analysis of whole-mount small intestinal epithelia of BALB/c mice. Confocal images stained with NKM 16-2-4-FITC, UEA-1-TRITC and WGA-AF633 are shown by green, red and blue, respectively. (A) Proximal villi (1) and PP (2), and distal villi (3, 5–8) and PP (4, 9–12) from naïve mice. (B) Proximal villi (13, 15–18) and PP (14), 1 day after oral CT administration. Arrows show villous M cells (NKM 16-2-4$^+$/UEA-1$^+$/WGA$^-$). Scale bars are 200 μm (1, 3, 13), 100 μm (2, 4, 14), 20 μm (5–12) or 10 μm (15–18). (For interpretation of the references to colour in this figure legend, the reader is referred to the web version of this article.)

2.7. Statistical analysis

The significance of the data was evaluated by the unpaired *t*-test, Mann–Whitney's U test, Tukey's or Scheffé's multiple comparison test based on the normality and variance of the data compared using Statcel2 software (OMS Publishing Inc., Saitama, Japan). $P < 0.05$ was considered statistically significant.

3. Results

3.1. Induction of α(1,2)fucosylation in the small intestinal epithelium by IES

To examine the influence of IES on M cell-associated α(1,2)fucosylation (NKM 16-2-4$^+$/UEA-1$^+$), we focused on the proximal epithelium, where NKM 16-2-4$^+$/UEA-1$^+$ cells were rarely found in naïve mice (Supplementary Fig. S1). When CT was orally administered to BALB/c mice, NKM 16-2-4$^+$/UEA-1$^+$ cells were dramatically increased in the proximal villous epithelium, with an average of 75.9% double-positive cells one day post-inoculation (Fig. 1A). The proportion of NKM 16-2-4$^+$/UEA-1$^+$ cells returned to the control level (approximately 2%) at 3 days post-inoculation. Similarly, a significant increase in NKM 16-2-4$^+$/UEA-1$^+$ cells was observed when pro-inflammatory agents, such as DSS or indomethacin, were administered (Fig. 1A).

A similar tendency was also seen in the FAE of PPs. We next performed histoplanimetrical analysis based on single NKM 16-2-4 signals obtained by CLSM. We previously demonstrated that NKM 16-2-4$^+$ cells included UEA-1$^+$ M cells but not goblet cells [22]. However, similar to UEA-1, because NKM 16-2-4 reacts to Paneth cells (Supplementary Fig. S2), NKM 16-2-4$^+$ cells were enumerated upward the crypts where Paneth cells locally exist. Therefore, goblet cells and Paneth cells were excluded in this analysis. When the proportions of NKM 16-2-4$^+$ cells were compared between the proximal and distal PP FAE of naïve BALB/c mice, a higher frequency of NKM 16-2-4$^+$ cells was observed in the distal (68.4%) than in the proximal (13.9%) PP FAE (Fig. 1B). Furthermore, a significant increase in NKM 16-2-4$^+$ cells was observed in the proximal PP FAE following CT-, DSS- or indomethacin-administration, averaging 27.2% (control: 18.1%), 33.8% (control: 13.9%) and 32.4% (control: 27.5%) positive cells, respectively (Fig. 1B). These results indicate that IES enhances α(1,2)fucosylation in both the PP FAE and the villous epithelium.

3.2. CLSM analysis of IES-induced NKM 16-2-4$^+$/UEA-1$^+$ cells

To assess qualitative cellular traits of IES-induced NKM 16-2-4$^+$/UEA-1$^+$ cells, we performed CLSM analysis using lectin WGA, which has an affinity for ECs and goblet cells but not M cells [6,8]. As indicated by FCM (Supplementary Fig. S1), a higher frequency of NKM 16-2-4$^+$/UEA-1$^+$ cells was observed in the distal (Fig. 2A; 3 and 4) than in the proximal villi and PPs (Fig. 2A; 1 and 2) in naïve BALB/c mice. In general, these NKM 16-2-4$^+$/UEA-1$^+$ cells were preferentially located at the tips of the villi (Fig. 2A; 1 and 3) and PP domes (Fig. 2A; 4) and a large proportion of them showed an affinity for WGA in both the villous epithelium (Fig. 2A; 7) and the PP FAE (Fig. 2A; 11), although a substantial number of villous M cells sharing the typical M cell hallmark (NKM 16-2-4$^+$/UEA-1$^+$/WGA$^-$) existed in the distal villi of naïve mice (Fig. 2A; 5–8: arrows).

The CLSM analysis further demonstrated that CT-induced NKM 16-2-4$^+$/UEA-1$^+$ cells also reacted with WGA (Fig. 2B). In contrast, villous M cells showing the M cell-phenotype (NKM 16-2-4$^+$/UEA-1$^+$/WGA$^-$) remained at a very low frequency irrespective of IES by CT (Fig. 2B; 15–18: arrows). A similar observation was made when DSS or indomethacin was administered (Supplementary Fig. S3). In the proximal PP FAE, whereas a substantial number of NKM 16-2-4$^+$/UEA-1$^+$ cells were negative for WGA and were radially distributed on the dome, indicating an M cell-phenotype (Fig. 2A; 2), triple-positive cells (NKM 16-2-4$^+$/UEA-1$^+$/WGA$^+$) were evident and were located on the tip of the dome after oral CT administration (Fig. 2B; 14). These results indicate that IES-induced NKM 16-2-4$^+$/UEA-1$^+$ cells share an affinity for WGA, a common trait of normal ECs [6], and hardly contain any villous M cells. We thus designated them fucosylated ECs (F-ECs), to distinguish them from typical M cells.

3.3. Different expression patterns of Fut1 and Fut2 transcripts in the small intestinal epithelium

To examine in more detail the mechanism of α(1,2)fucosylation between F-ECs and M cells, we performed quantitative real-time RT-PCR for *Fut1* and *Fut2* transcripts. Quantitative real-time RT-PCR demonstrated that high expression of *Fut1* transcripts was seen only in NKM 16-2-4$^+$/UEA-1$^+$ cells isolated from the naïve PP FAE where M cells predominantly exist (Fig. 3A). On the other hand, elevated expression of *Fut2* transcripts, but not *Fut1* transcripts, was detected in F-ECs located in the distal epithelia of naïve mice (Fig. 3A and B). Similarly, enhanced expression of *Fut2* transcripts, but not *Fut1* transcripts, was seen in CT-, DSS- and indomethacin-induced F-ECs of the proximal epithelia (Fig. 3A and B). These results indicate that α(1,2)fucosylation of F-ECs in the villous epithelium is induced by Fut2, and suggest that Fut1 is expressed in PP M cells irrespective of IES.

3.4. Distinct requirements for Fut1 or Fut2 for α(1,2)fucosylation of M cells or F-ECs, respectively

To clarify the distinct requirements for the Fut isoforms in F-ECs and M cells, Fut1-null and Fut2-null mice were employed for FCM

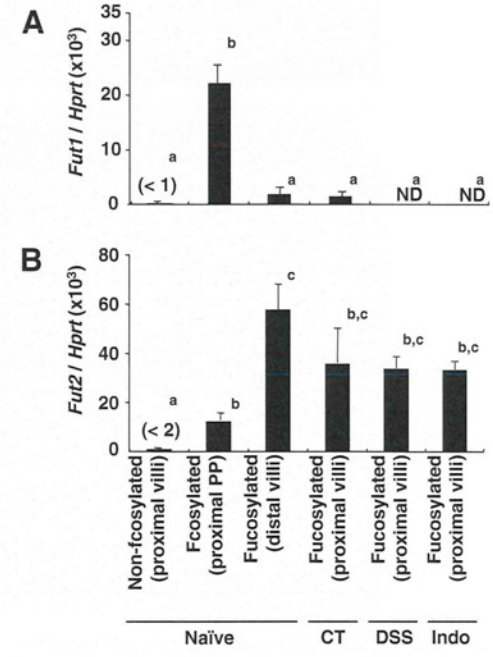

Fig. 3. Quantification of the expression levels of *Fut1* and *Fut2* transcripts relative to levels of *Hprt* transcripts. Fucosylated (NKM 16-2-4$^+$/UEA-1$^+$) and non-fucosylated (UEA-1$^-$) cells were purified from the proximal or distal small intestinal epithelia using a cell-sorter. Naïve, or CT- (Day 2), DSS- (Day 7) or indomethacin (Indo)- (Day 2) treated BALB/c mice were used. (A) *Fut1* transcripts. (B) *Fut2* transcripts. Data are given as means ± SE ($n = 3$–4). Different letters indicate significant differences ($P < 0.05$) determined by Tukey's multiple comparison test.

and CLSM analyses. Because these mice are on a C57BL/6J background [21], wild-type (WT) C57BL/6J mice were employed as a control group. Like BALB/c mice, WT C57BL/6J mice showed a higher frequency of F-ECs (NKM 16-2-4$^+$/UEA-1$^+$ cells) in the distal villous epithelium than in the proximal villous epithelium, and that the frequency of F-ECs in the latter increased after oral CT administration (Fig. 4A). This was also observed when Fut1-null mice were orally exposed to CT (Fig. 4A and C; 2 and 4). On the

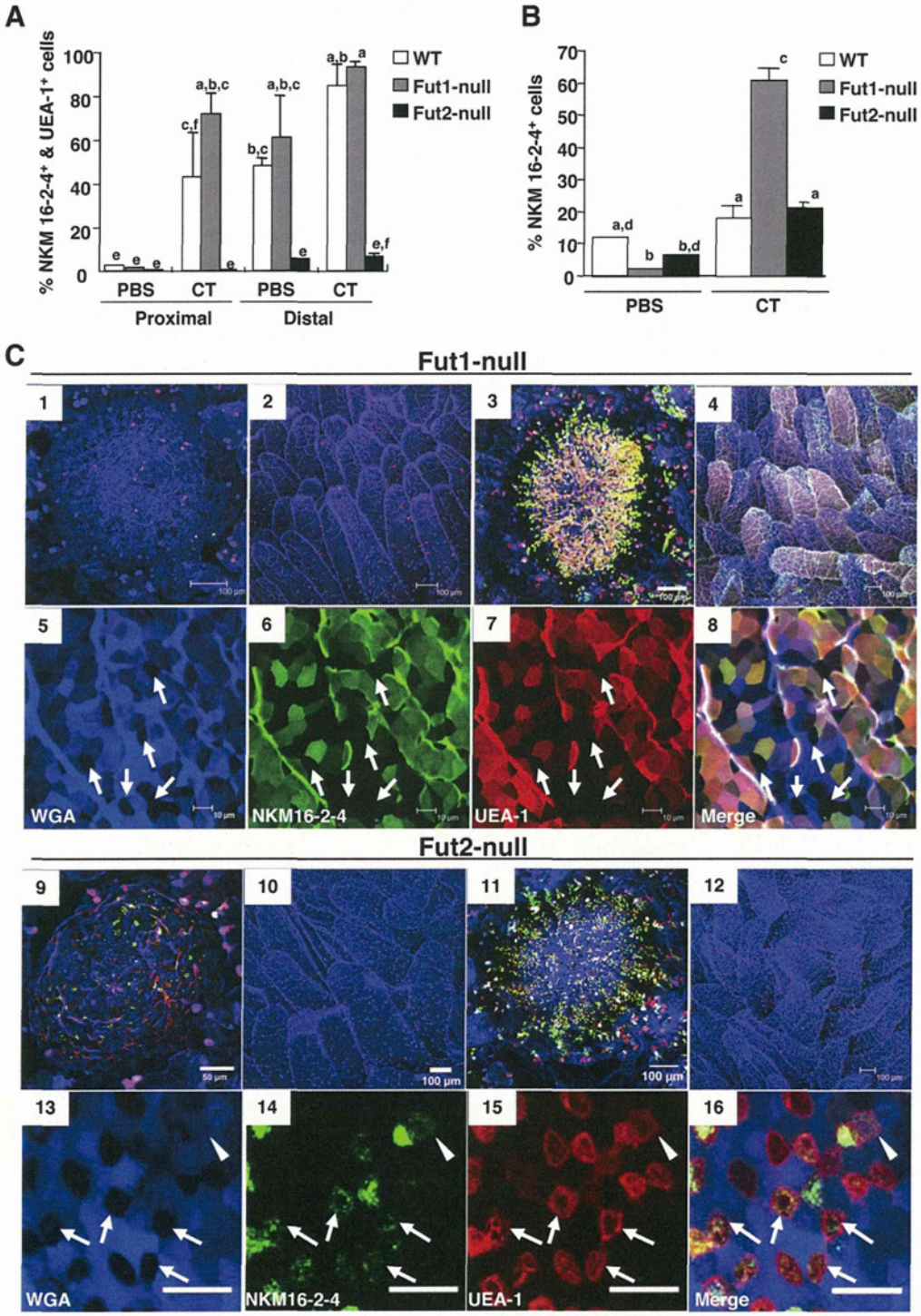

Fig. 4. Fut1- and Fut2-dependent α(1,2)fucosylation in PP M cells and F-ECs, respectively. (A) The proportions of NKM 16-2-4$^+$/UEA-1$^+$ cells in the proximal and distal villous epithelia of either day 1 PBS- or CT-administered (CT) WT C57BL/6J, Fut1-null and Fut2-null mice based on FCM as described in the Fig. 1 legend. Data are given as means ± SE (n = 3). Different letters indicate significant differences (P < 0.05) determined by Tukey's multiple comparison test. (B) The proportions of NKM 16-2-4$^+$ cells in the proximal PP domes based on histoplanimetrical analysis of CLSM images. WT, Fut1-null and Fut2-null mice were used after oral administration of either PBS or CT (day 1). Data are given as means ± SE (n = 3, 12–25 domes). Different letters indicate significant differences (P < 0.05) determined by Scheffé's multiple comparison test. (C) CLSM analysis for the whole-mount small intestinal epithelia of either naïve or day 1 CT-treated Fut1-null (naïve; 1, 2, CT; 3–8) and Fut2-null mice (naïve; 9, 10, CT; 11–16). Confocal images stained with NKM 16-2-4-FITC, UEA-1-TRITC and WGA-AF633 are shown by green, red and blue, respectively. Arrows and arrowheads indicate WGA$^-$ PP M cells and Fut1-dependent WGA$^+$ cells, respectively. Scale bars are 100 μm (1–4, 10–12), 50 μm (9), 20 μm (13–16) or 10 μm (5–8). (For interpretation of the references to colour in this figure legend, the reader is referred to the web version of this article.)

other hand, Fut2-null mice possessed few NKM 16-2-4$^+$/UEA-1$^+$ cells in the villous epithelia and the number of these cells was not increased upon oral CT administration (Fig. 4A and C; 10 and 12). PBS-administered Fut2-null mice showed 0.1% and 4.9% of NKM 16-2-4$^+$/UEA-1$^+$ cells in the proximal and distal villous epithelia, respectively, and CT-administered Fut2-null mice showed 0.3% and 5.3% in the proximal and distal villous epithelia, respectively (Fig. 4A).

In contrast to the villous epithelia, the PP FAE contained both types of fucosylated cells, dependent on either Fut1 or Fut2. In PBS-administered conditions, 2.0% and 6.3% of NKM 16-2-4$^+$ cells were observed in the proximal PP FAE of Fut1-null and Fut2-null mice, respectively (Fig. 4B). Oral CT administration did not notably induce α(1,2)fucosylation in the PP FAE of WT mice; CT-administered and PBS-administered WT mice contained 17.8% and 12.0% of NKM 16-2-4$^+$ cells, respectively, and there was no statistical difference between the two groups (Fig. 4B). However, both Fut1-null and Fut2-null mice showed significant induction of NKM 16-2-4$^+$ cells in the proximal PP FAE, with the proportion of positive cells being 60.5% and 21.0%, respectively (Fig. 4B). CLSM analysis further revealed that the fucosylation of M cells was dependent on Fut1, because WGA$^-$ M cells did not induce α(1,2)fucosylation and thus did not react with either NKM 16-2-4 or UEA-1 in Fut1-null mice (Fig. 4C; 1, 3 and 5–8: arrows) whereas they did react with these markers in Fut2-null mice (Fig. 4C; 9, 11 and 13–16: arrows) irrespective of oral CT administration. In addition, the fucosylation of F-ECs in the PP FAE was dependent on Fut2 because triple-positive cells (NKM 16-2-4$^+$/UEA-1$^+$/WGA$^+$ cells) were preferentially observed in the CT-administered Fut1-null mice (Fig. 4C; 3 and 5–8). Although a small number of Fut1-dependent WGA$^+$ cells were observed in the PP FAE of CT-administered Fut2-null mice (Fig. 4C; 13–16: arrowheads), they were distributed radially, accompanying abundant WGA$^-$ M cells on the PP dome (Fig. 4C; 11), and were distinguishable from the Fut2-dependent F-ECs that were distributed all over the dome (Fig. 4C; 3).

Taken together, these results indicate that α(1,2)fucosylation of PP M cells is dependent on Fut1 irrespective of IES, and that Fut2 is involved in α(1,2)fucosylation of F-ECs residing in both the PP FAE and villous epithelium in response to IES.

4. Discussion

In this study, we showed that intestinal environmental and biological stress induced F-ECs, which were recognized by NKM 16-2-4 and UEA-1, in both the PP FAE and the villous epithelium. However, such IES-induced F-ECs possessed a strong affinity for WGA (Fig. 2). In addition, F-ECs showed the same morphological characteristics as ECs such as columnar architecture, well-developed tall and dense microvilli (Supplementary Fig. S4), and did not possess *Salmonella* uptake-ability (Supplementary Fig. S5). Furthermore, F-ECs did not express glycoprotein 2 (Supplementary Fig. S6 and Table S1), recently identified as an M cell-specific molecule [17,25]. Therefore, F-ECs should be distinguished from typical M cells, and IES-induced α(1,2)fucosylation reflects only a phenotypic change of surface glycosylation pattern that is irrelevant to M-cell differentiation.

The requirements for different fucosylation-inducing enzymes clearly demonstrated a distinction between F-ECs and PP M cells: Fut1 is essential for the fucosylation associated with PP M cells while Fut2 is specifically involved in the fucosylation of IES-induced F-ECs in both the PP FAE and villous epithelium (Fig. 4). Although it has been reported that the expression of *Fut1* transcripts is rare and is not induced or altered in the small intestine by the transfer from germ-free to conventional conditions [11,18–20], these results are probably due to the low frequency of PP M cells throughout the small intestine. In contrast, it has been known that *Fut2* transcripts are induced in the small intestine, particularly in the ileum, of mice in response to colonization by commensal bacteria or treatment with a protein synthesis inhibitor [11,19]. Our present data, in which IES resulted in the induction of Fut2-dependent F-ECs, is consistent with and support these previous findings.

Fut1 and Fut2 provide insights into the involvement of IES in the development of not only F-ECs but also M cells. The PP dome epithelium consists of two cell lineages: one is derived from the dome-associated crypts and differentiates into either M cells or ECs, and the other is derived from villus-associated crypts and differentiates into ECs [26]. In addition, some studies have revealed a dynamic and plastic morphology of M cells; for example, the distinctive microfold and membranous structures occur transiently during the cell differentiation process, and M cell-lineage cells in their early and terminal development stages show the same morphological structure as ECs [27,28]. In this study, we showed a possibility that Fut1-dependent fucosylated cells are increased by IES (Fig. 4). These cells consisted of abundant PP M cells and a few WGA$^+$ EC-like cells, both of which were distributed radially on the dome. To this end, we suggest a possibility that Fut1-dependent cells are M cell-lineage cells derived from the dome-associated crypts that participate in the increase of M cells in response to IES, as described elsewhere [12–15]. In contrast to PP M cells, the fucosylation of villous M cells, like F-ECs, is regulated by Fut2 because α(1,2)fucosylation in the villi was not observed in Fut2-null but Fut1-null mice regardless of oral CT administration (Fig. 4 and Supplementary Table S1). However, IES alone would not influence the frequency of villous M cells because oral CT administration did not induce *Salmonella* uptake in the villi (Supplementary Fig. S5). It has recently been shown that receptor activator of nuclear factor-kappa B ligand (RANKL) is capable of the full development of both PP and villous M cells but RANKL-expressing inducer cells preferentially exist in the subepithelial dome of PPs [29]. Taken together, transient IES alone might be insufficient for the recruitment and/or induction of RANKL-expressing cells in the villi, and/or other factors might be required for the full development of villous M cells.

Although specific functions of F-ECs remain to be elucidated, our present study offers the possibility that Fut1-null and Fut2-null mice would provide a direct opportunity to examine *in vivo* the immuno-biological role of F-ECs and M cells, including their specific fucosylated glycans, towards a better understanding of the gut mucosal immune system.

Acknowledgments

We thank Dr. Osamu Igarashi for technical support and Dr. Rebecca Devon for editing the manuscript. This work was supported in part by Grants from the Ministry of Education, Science, Sports and Culture of Japan (H.K. and K.T.), and the Ministry of Health, Labour and Welfare of Japan (H.K.).

Appendix A. Supplementary data

Supplementary data associated with this article can be found, in the online version, at doi:10.1016/j.bbrc.2010.12.067.

References

[1] M.R. Neutra, A. Frey, J.P. Kraehenbuhl, Epithelial M cells: gateways for mucosal infection and immunization, Cell 86 (1996) 345–348.
[2] H. Hamada, T. Hiroi, Y. Nishiyama, et al., Identification of multiple isolated lymphoid follicles on the antimesenteric wall of the mouse small intestine, J. Immunol. 168 (2002) 57–64.
[3] R.L. Owen, A.L. Jones, Epithelial cell specialization within human Peyer's patches: an ultrastructural study of intestinal lymphoid follicles, Gastroenterology 66 (1974) 189–203.

[4] M.R. Neutra, N.J. Mantis, A. Frey, et al., The composition and function of M cell apical membranes: implications for microbial pathogenesis, Semin. Immunol. 11 (1999) 171–181.
[5] J.P. Kraehenbuhl, M.R. Neutra, Epithelial M cells: differentiation and function, Annu. Rev. Cell Dev. Biol. 16 (2000) 301–332.
[6] M.A. Clark, M.A. Jepson, N.L. Simmons, et al., Differential expression of lectin-binding sites defines mouse intestinal M-cells, J. Histochem. Cytochem. 41 (1993) 1679–1687.
[7] M.A. Clark, M.A. Jepson, N.L. Simmons, et al., Selective binding and transcytosis of Ulex europaeus 1 lectin by mouse Peyer's patch M-cells in vivo, Cell Tissue Res. 282 (1995) 455–461.
[8] M.H. Jang, M.N. Kweon, K. Iwatani, et al., Intestinal villous M cells: an antigen entry site in the mucosal epithelium, Proc. Natl. Acad. Sci. USA 101 (2004) 6110–6115.
[9] Y. Umesaki, M. Ohara, Factors regulating the expression of the neutral glycolipids in the mouse small intestinal mucosa, Biochim. Biophys. Acta 1001 (1989) 163–168.
[10] L. Bry, P.G. Falk, T. Midtvedt, et al., A model of host-microbial interactions in an open mammalian ecosystem, Science 273 (1996) 1380–1383.
[11] B. Lin, Y. Hayashi, M. Saito, et al., GDP-fucose: beta-galactoside alpha1,2-fucosyltransferase, MFUT-II, and not MFUT-I or -III is induced in a restricted region of the digestive tract of germ-free mice by host-microbe interactions and cycloheximide, Biochim. Biophys. Acta 1487 (2000) 275–285.
[12] M.W. Smith, P.S. James, D.R. Tivey, M cell numbers increase after transfer of SPF mice to a normal animal house environment, Am. J. Pathol. 128 (1987) 385–389.
[13] T.C. Savidge, M.W. Smith, P.S. James, et al., Salmonella-induced M-cell formation in germ-free mouse Peyer's patch tissue, Am. J. Pathol. 139 (1991) 177–184.
[14] C. Borghesi, M.J. Taussig, C. Nicoletti, Rapid appearance of M cells after microbial challenge is restricted at the periphery of the follicle-associated epithelium of Peyer's patch, Lab. Invest. 79 (1999) 1393–1401.
[15] T. Kucharzik, A. Lugering, N. Lugering, et al., Characterization of M cell development during indomethacin-induced ileitis in rats, Aliment. Pharmacol. Ther. 14 (2000) 247–256.
[16] J. Mach, T. Hshieh, D. Hsieh, et al., Development of intestinal M cells, Immunol. Rev. 206 (2005) 177–189.
[17] K. Terahara, M. Yoshida, O. Igarashi, et al., Comprehensive gene expression profiling of Peyer's patch M cells, villous M-like cells and intestinal epithelial cells, J. Immunol. 180 (2008) 7840–7846.
[18] S.E. Domino, N. Hiraiwa, J.B. Lowe, Molecular cloning, chromosomal assignment and tissue-specific expression of a murine alpha(1,2)-fucosyltransferase expressed in thymic and epididymal epithelial cells., Biochem. J. 327 (Pt 1) (1997) 105–115.
[19] M. Iwamori, S.E. Domino, Tissue-specific loss of fucosylated glycolipids in mice with targeted deletion of alpha(1, 2)fucosyltransferase genes, Biochem. J. 380 (2004) 75–81.
[20] B. Lin, M. Saito, Y. Sakakibara, et al., Characterization of three members of murine alpha1,2-fucosyltransferases: change in the expression of the Se gene in the intestine of mice after administration of microbes, Arch. Biochem. Biophys. 388 (2001) 207–215.
[21] S.E. Domino, L. Zhang, P.J. Gillespie, et al., Deficiency of reproductive tract alpha(1,2)fucosylated glycans and normal fertility in mice with targeted deletions of the FUT1 or FUT2 alpha(1,2)fucosyltransferase locus, Mol. Cell. Biol. 21 (2001) 8336–8345.
[22] T. Nochi, Y. Yuki, A. Matsumura, et al., A novel M cell-specific carbohydrate-targeted mucosal vaccine effectively induces antigen-specific immune responses, J. Exp. Med. 204 (2007) 2789–2796.
[23] I. Okayasu, S. Hatakeyama, M. Yamada, et al., A novel method in the induction of reliable experimental acute and chronic ulcerative colitis in mice, Gastroenterology 98 (1990) 694–702.
[24] T. Kunikata, H. Araki, M. Takeeda, et al., Prostaglandin E prevents indomethacin-induced gastric and intestinal damage through different EP receptor subtypes, J. Physiol. Paris 95 (2001) 157–163.
[25] K. Hase, K. Kawano, T. Nochi, et al., Uptake through glycoprotein 2 of FimH(+) bacteria by M cells initiates mucosal immune response, Nature 462 (2009) 226–230.
[26] A. Gebert, S. Fassbender, K. Werner, et al., The development of M cells in Peyer's patches is restricted to specialized dome-associated crypts, Am. J. Pathol. 154 (1999) 1573–1582.
[27] S. Onishi, T. Yokoyama, K. Chin, et al., Ultrastructural study on the differentiation and the fate of M cells in follicle-associated epithelium of rat Peyer's patch, J. Vet. Med. Sci. 69 (2007) 501–508.
[28] F. Sierro, E. Pringault, P.S. Assman, et al., Transient expression of M-cell phenotype by enterocyte-like cells of the follicle-associated epithelium of mouse Peyer's patches, Gastroenterology 119 (2000) 734–743.
[29] K.A. Knoop, N. Kumar, B.R. Butler, et al., RANKL is necessary and sufficient to initiate development of antigen-sampling M cells in the intestinal epithelium, J. Immunol. 183 (2009) 5738–5747.

THE JOURNAL OF IMMUNOLOGY

In Vivo Molecular Imaging Analysis of a Nasal Vaccine That Induces Protective Immunity against Botulism in Nonhuman Primates

Yoshikazu Yuki, Tomonori Nochi, Norihiro Harada, Yuko Katakai, Hiroaki Shibata, Mio Mejima, Tomoko Kohda, Daisuke Tokuhara, Shiho Kurokawa, Yuko Takahashi, Fumiko Ono, Shunji Kozaki, Keiji Terao, Hideo Tsukada and Hiroshi Kiyono

J Immunol 2010; 185:5436-5443; Prepublished online 29 September 2010;
doi: 10.4049/jimmunol.1001789
http://www.jimmunol.org/content/185/9/5436

The Journal of Immunology is published twice each month by The American Association of Immunologists, Inc., 9650 Rockville Pike, Bethesda, MD 20814-3994.

Print ISSN: 0022-1767 Online ISSN: 1550-6606.

In Vivo Molecular Imaging Analysis of a Nasal Vaccine That Induces Protective Immunity against Botulism in Nonhuman Primates

Yoshikazu Yuki,*[,1] Tomonori Nochi,*[,1] Norihiro Harada,[†] Yuko Katakai,[‡] Hiroaki Shibata,[§] Mio Mejima,* Tomoko Kohda,[¶] Daisuke Tokuhara,* Shiho Kurokawa,* Yuko Takahashi,* Fumiko Ono,[‡] Shunji Kozaki,[¶] Keiji Terao,[§] Hideo Tsukada,[†] and Hiroshi Kiyono*

Nasal administration is an effective route for a needle-free vaccine. However, nasally administered Ags have the potential to reach the CNS directly from the nasal cavity, thus raising safety concerns. In this study, we performed real-time quantitative tracking of a nasal vaccine candidate for botulism, which is a nontoxic subunit fragment of *Clostridium botulinum* type A neurotoxin (BoHc/A) effective in the induction of the toxin-neutralizing immune response, by using ^{18}F-labeled BoHc/A–positron-emission tomography, an in vivo molecular imaging method. This method provides results that are consistent with direct counting of [^{18}F] radioactivity or the traditional [^{111}In]-radiolabel method in dissected tissues of mice and nonhuman primates. We found no deposition of BoHc/A in the cerebrum or olfactory bulb after nasal administration of ^{18}F-labeled BoHc/A in both animals. We also established a real-time quantitative profile of elimination of this nasal vaccine candidate and demonstrated that it induces highly protective immunity against botulism in nonhuman primates. Our findings demonstrate the efficiency and safety of a nasal vaccine candidate against botulism in mice and nonhuman primates using in vivo molecular imaging. *The Journal of Immunology*, 2010, 185: 5436–5443.

Nasal administration is one of the most effective routes for the induction of Ag-specific protective immunity in both systemic and mucosal compartments. A nasally delivered, live attenuated influenza vaccine, FluMist, was recently approved in the United States (1); however, an inactivated nasal influenza vaccine with a heat-labile enterotoxin adjuvant was associated with facial paralysis in a study in Switzerland (2). Toxin-based adjuvants, composed of cholera toxin or cholera toxin B subunit, are redirected to the olfactory bulb (OB) in the CNS when administered via the nasal route in mouse (3). The results of this mouse study suggest that the deposition of vaccine or adjuvant, or both, in the CNS via the nasal route might cause adverse effects. Thus, a key issue to investigate during nasal vaccine development is whether a candidate vaccine, with or without adjuvant, could reach the CNS. Tracking of nasally administered vaccines should take into account the anatomical differences between mice and humans in the olfactory epithelium of nasal cavity. Mice and dogs harbor well-developed olfactory epithelium that covers 70–80% of the total surface area of the nasal cavity, whereas that of nonhuman primates and humans covers only ~10% of the total surface area of the nasal cavity (4). Therefore, the evaluation of a nasal vaccine by safety pharmacology studies, such as absorption, distribution, metabolism, and excretion (ADME) studies, must be performed in multiple species, including nonhuman primates, before clinical trials in humans.

Traditionally, the evaluation of ADME in the development of biotechnology-derived pharmaceuticals has involved autoradiography of the whole body and the detection of radioactivity associated with dissected tissues by means of radioactive ^{125}I- or ^{111}In-labeled pharmaceuticals (5). However, recent molecular imaging technologies allow visualization and quantitative measurement of biological processes in living systems (6, 7). Radioisotope-based molecular imaging techniques, such as positron-emission tomography (PET), have been used for the noninvasive detection of pathological changes in cancer and to ascertain functional changes in the nervous system (8, 9). Hybrid technologies combining PET imaging with traditional structural imaging techniques, such as computerized tomography (CT) scanning and magnetic resonance

*Division of Mucosal Immunology, Department of Microbiology and Immunology, Institute of Medical Science, University of Tokyo, Tokyo; [†]PET Center, Central Research Laboratory, Hamamatsu Photonics K.K., Shizuoka; [‡]Corporation for Production and Research of Laboratory Primates; [§]Tsukuba Primate Research Center, National Institute of Biomedical Innovation, Ibaraki; and [¶]Laboratory of Veterinary Epidemiology, Department of Veterinary Science, Graduate School of Life and Environmental Sciences, Osaka Prefecture University, Osaka, Japan

[1]Y.Y. and T.N. contributed equally to this work.

Received for publication June 4, 2010. Accepted for publication August 29, 2010.

This work was supported by the Research and Development Program for New Bio-industry Initiatives of the Bio-oriented Technology Research Advancement Institution and a Grant-in-Aid from the Ministry of Education, Culture, Sports, Science and Technology (to Y.Y.), a research fellowship of the Japan Society for the Promotion of Science (to T.N.), the Core Research for Engineering, Science, and Technology, Japan Science and Technology Agency (to H.T.), a Grant-in-Aid from the Ministry of Health and Welfare of Japan and the Global Centers of Excellence Program, Center of Education and Research for the Advanced Genome-based Medicine for Personalized Medicine and the Control of Worldwide Infectious Diseases, and an Academic Frontier Project for Private Universities matching-fund subsidy from the Ministry of Health and Welfare of Japan (to H.K).

Address correspondence and reprint requests to Drs. Hiroshi Kiyono and Yoshikazu Yuki, Division of Mucosal Immunology, Department of Microbiology and Immunology, Institute of Medical Science, University of Tokyo, 4-6-1 Shirokanedai, Minato-ku, Tokyo 108-8639, Japan. E-mail addresses: kiyono@ims.u-tokyo.ac.jp and yukiy@ims.u-tokyo.ac.jp

The online version of this article contains supplemental material.

Abbreviations used in this paper: ADME, absorption, distribution, metabolism, and excretion; BoHc/A, nontoxic subunit fragment of *Clostridium botulinum* type A neurotoxin; BoNT/A, *C. botulinum* neurotoxin type A; CT, computerized tomography; EOB, end of bombardment; [^{18}F]-BoHc/A, ^{18}F-labeled BoHc/A; [^{18}F]SFB, *N*-succinimidyl-4-[^{18}F]fluorobenzoate; MIP, maximum intensity projection; MRI, magnetic resonance imaging; NALT, nasopharynx-associated lymphoid tissue; N.D., not determined; OB, olfactory bulb; PD-10, prepacked disposable; PET, positron-emission tomography; PPIS, planar positron whole-body imaging system; SUV, standardized uptake value; TAC, time-activity curve.

www.jimmunol.org/cgi/doi/10.4049/jimmunol.1001789

imaging (MRI), have improved the sensitivity and specificity of these analyses (10).

PET imaging agents usually consist of small-molecule tracers, such as glucose analogs or neuroreceptor ligands (9), and rarely consist of proteins (11). In this study, we attempted to develop a PET imaging system that uses a protein tracer for evaluating nasal vaccine candidates in multiple species. For this approach, we chose to evaluate a recombinant form of the nontoxic fragment of the C-terminal half of the H chain of *Clostridium botulinum* type A neurotoxin (BoHc/A) as a subunit vaccine candidate against botulism (12). It has been shown that systemic immunization of primates with a similar preparation of type B (BoHc/B) resulted in the generation of neutralizing Ab response (13). Because of the potential for botulinum neurotoxin to be disseminated by bioterrorists via airborne or oral routes and to result in a high mortality rate, it was classified as a category A agent by the U.S. Centers for Disease Control and Prevention. Thus, the development of an effective nasal vaccine against botulism is considered a potent strategy to prevent inhalation and gastrointestinal botulism (14).

In this paper, we show that a nasal BoHc/A vaccine candidate provided full protective immunity against toxin-based neurologic complications in nonhuman primates. To assess the safety issue of redirection of the Ag to the CNS, we developed PET with ^{18}F-labeled BoHc/A ([^{18}F]-BoHc/A) and evaluated the ADME of the nasal BoHc/A vaccine in both mice and nonhuman primates. In contrast with traditional whole-body autoradiography, the use of PET in combination with CT or MRI allowed noninvasive and dynamic in vivo quantitative imaging of [^{18}F]-BoHc/A. Both PET and direct tissue counting showed no evidence of CNS deposition of the vaccine Ag in the cerebrum or OB after nasal administration of [^{18}F]-BoHc/A or the more traditional [^{111}In]-BoHc/A in mice and nonhuman primates.

Materials and Methods

Preparation of C. botulinum *neurotoxin type A*

C. botulinum neurotoxin type A (BoNT/A) from *C. botulinum* type A 62 was purified from the culture supernatant as previously described (15). The toxicity of purified BoNT/A (1.1×10^8 mouse i.p. LD_{50}/mg protein) was assayed by time to death after i.v. injection into mice (16).

Preparation of botulinum mucosal vaccine (BoHc/A)

The gene coding the nontoxic C-terminal fragment of H chain of type A botulinum neurotoxin (strain 62A; aa 872–1296), BoHc/A, was synthesized by PCR with Phusion High-Fidelity polymerase (Daiichi Pure Chemicals, Tokyo, Japan) and specific primers (sense, 5′-CGTCGGGATCCAATATTATTAATACTTCTATATTG-3′; antisense, 5′-TAGTAGTCGACTTACAGTGGCCTTTCTCCCCATCC-3′; BamHI and SalI restriction enzyme sites shown by underlining). After digestion with BamHI and SalI, the gene fragment was inserted into the plasmid pGEX-6P3 (GE Healthcare, Piscataway, NJ). After DNA sequencing, the plasmid was used to transform Rosetta 2(DE3) pLysS cells (Novagen, Madison, WI), and the cells were treated with 0.1 mM isopropyl-β-D-thiogalactopyranoside for 4 h at 28°C to induce BoHc/A expression. The cells were then suspended in PBS and sonicated on ice. After centrifugation, the supernatant was loaded onto a DEAE Sepharose column (GE Healthcare) in PBS. To purify the GST-fused BoHc/A protein, we loaded the pass-through fraction onto a glutathione Sepharose column (GE Healthcare) in PBS. The fusion protein on the column was treated with PreScission Protease (GE Healthcare) overnight at 4°C to cleave between GST and BoHc/A, and the digested fraction containing BoHc/A was collected. Finally, purification by gel filtration on a Sephacryl S-100 (GE Healthcare) column was performed. Purified BoHc/A was confirmed by liquid chromatography/mass spectrometry (LC/MS-MS; Applied Biosystems, Foster City, CA) analysis after treatment with trypsin gold (Promega, Madison, WI). The level of LPS contamination in the purified BoHc/A (<10 endotoxin units/mg protein) was measured by using the *Limulus* J Single Test (Wako, Osaka, Japan).

Synthesis of [^{18}F]-BoHc/A and [^{18}F]-cholera toxin

[^{18}F]-BoHc/A was labeled with *N*-succinimidyl-4-[^{18}F]fluorobenzoate ([^{18}F]SFB). In brief, [^{18}F]fluoride was produced by the 18O(p, n)[^{18}F] nuclear reaction by the use of a cyclotron (HM-18; Sumitomo Heavy Industries, Tokyo, Japan) at Hamamatsu Photonics PET Center. [^{18}F]SFB was prepared from 4-(trimethylammonium triflate) benzoate (17) and [^{18}F]KF/K[2,2,2] according to the procedure of Tang et al. (18) with some modifications. [^{18}F]KF/K[2,2,2] complex was added to 5 mg of the precursor in 1.5 ml acetonitrile (CH_3CN) and reacted at 80°C for 10 min. After cooling the reaction mixture, 20 μl 1M tetra-*n*-propyl-ammonium hydroxide (Pr_4NOH) in 0.5 ml CH_3CN was added and hydrolyzed at 120°C for 5 min. N,N,N′,N′-tetramethyl-*O*-(N-succinimidyl)uranium tetrafluoroborate (15 mg) in 0.5 ml CH_3CN was added to the reaction mixture and reacted at 80°C for 5 min to produce [^{18}F]SFB. The reaction mixture was diluted with 1.5 ml of 5% acetic acid (CH_3COOH) and transferred to an HPLC injector. An extra 1.5 ml of 5% CH_3COOH was used to rinse the reaction vessel. The combined crude product was purified by semi-preparative HPLC (HPLC conditions: Inertsil ODS-3 column, CH_3CN:H_2O = 300:700, 6 ml/min, detection: 254 nm). The radioactive peak that eluted at 13.5 min was collected, diluted with 30 ml H_2O, and passed through a Sep-Pak C18 cartridge (Nihon Waters K.K., Tokyo, Japan). The [^{18}F]SFB retained on the cartridge was released with 4 ml CH_2Cl_2 and recovered to a V-vial through a Sep-Pak Dry cartridge (Nihon Waters). The decay-corrected radiochemical yield of [^{18}F]SFB was 28.1–38.3% (average, 33.5%; $n = 4$), based on [^{18}F]fluoride, and the radiochemical purity was >99%. The [^{18}F]SFB was then concentrated at 60°C under He flow (200 ml/min) and used directly for next step. [^{18}F]SFB was added to a solution of 0.5 M borate buffer (pH 8.5, 200 μl), PBS (100 μl), BoHc/A (4.1 mg/ml, 200 μl), and allowed to react at room temperature for 30 min. Purified BoHc/A was successfully radiolabeled by conjugation with [^{18}F]SFB, which reacted with free amino groups including an N-terminal and ε–Lys amino groups in the protein. The product was purified by gel-permeation chromatography (Superose 12, PBS, 1 ml/min), and the radioactive peak eluted at 13.5 min was collected. The 373–698 MBq (average, 548 MBq; $n = 4$) [^{18}F]-BoHc/A was obtained in 140 min from the end of bombardment (EOB). The radiochemical purity from EOB was 100%, and the decay-corrected radiochemical yield from EOB was 2.8–4.5% (average, 3.7%; $n = 4$). The sp. act. was 1.91–2.85 MBq/μg protein (average, 2.46 MBq/μg protein; $n = 4$). Cholera toxin (List Biological Laboratories, Campbell, CA) was similarly radiolabeled by conjugation with [^{18}F]SFB and purified by the HPLC. The 126 MBq [^{18}F]-cholera toxin was obtained in 150 min from EOB. The radiochemical purity from the EOB was 100%, and the decay-corrected radiochemical yield from EOB was 0.85%. The sp. act. of the [^{18}F]-cholera toxin was 1.42 MBq/μg protein.

Preparation of [^{111}In]-BoHc/A and [^{111}In]-cholera toxin

BoHc/A and cholera toxin (List Biological Laboratories) were labeled with indium chloride ([^{111}In], half-life 2.805 d; Nihon Medi-Physics, Tokyo, Japan) anhydride (Dojindo, Kumamoto, Japan) via N-terminal and ε–Lys amino groups using DTPA as described previously (19). The sp. act. of [^{111}In]-BoHc/A and [^{111}In]-cholera toxin were 638,000–915,000 (average, 775,000 cpm/μg protein; $n = 4$) and 825,000–909,000 cpm/μg protein (average, 867,000 cpm/μg protein; $n = 2$), respectively.

Animals

Female BALB/c mice (4–7 wk old) purchased from Japan SLC (Shizuoka, Japan) were used for the direct radioactive counting in tissues after nasal administration of [^{111}In]-BoHc/A at the Institute of Medical Science of The University of Tokyo, and for PET/CT imaging and direct radioactive counting in tissues after nasal administration of [^{18}F]-BoHc/A at PET Center of Hamamatsu Photonics K.K. For the primate study, two groups of monkey housed in two different research centers were used. Four female naive cynomolgus macaques (*Macaca fascicularis*, 5 y old, ~3 kg) were used for the immunization/challenge study and were maintained at the Tsukuba Primate Research Center for Medical Science in National Institute of Biomedical Innovation (NIBIO, Ibaraki, Japan). In the separate experiment, two male and naive rhesus macaques (*Macaca mulatta*, 5–6 y old, ~5 kg) were used for the PET imaging study at PET Center of Hamamatsu Photonics K.K. All experiments were performed according to the guidelines provided by the Animal Care and Use Committee of The University of Tokyo, Hamamatsu Photonics K.K., and NIBIO.

PET/CT imaging in mice

After nasal administration of 0.90 MBq (0.34 μg) per 20 μl [^{18}F]-BoHc/A (10 μl, each nostril), mice were anesthetized by i.p. injection of chloral hydrate (300 mg/kg i.p.) and placed in a small-animal PET scanner

(Clairvivo-PET; Shimadzu, Kyoto, Japan) (20). Scans were conducted for 10 h. A CT scan was obtained by using a small-animal CT scanner (Clairvivo-CT; Shimadzu) after the PET scan to identify organs and tissues.

Planar positron whole-body imaging system imaging in mice

Mice (n = 2) were fixed on an acrylic plate with thread and surgical tape (two animals on each acrylic plate) after nasal administration of 0.90 MBq (0.34 μg) per 20 μl [^{18}F]-BoHc/A. Mice with an acrylic plate were placed at the center position between two planar positron whole-body imaging system (PPIS) detectors and scans with 10-min time frame were performed for 10 h with 60 × 10-min frame using a planar positron imaging system (PPIS-4800; Hamamatsu Photonics, Hamamatsu, Japan) (21). PPIS data were analyzed by using ImageJ software and expressed as counts per pixel. Time-activity curves (TACs) of planar images were expressed as total counts in region of interest.

Analyses of radiolabeled-BoHc/A and cholera toxin in dissected tissues in mice

After nasal administration of 0.90 MBq (0.34 μg) per 20 μl [^{18}F]-BoHc/A or 0.56 MBq (0.39 μg) per 20 μl [^{18}F]-cholera toxin to mice (n = 3 at indicated time), the radioisotope counts in various tissues were directly measured by a gamma counter (1480 Wizard; PerkinElmer, Waltham, MA), and the values were adjusted for tissue weight to provide standardized uptake values (SUVs), at the times indicated in Fig. 2*A–C*. A similar procedure was carried out after nasal administration of mice (n = 3 at indicated time) with 1 × 10^6 cpm (1.1 μg) per 18 μl [^{111}In]-BoHc/A or 1 × 10^6 cpm (1.1 μg) per 20 μl [^{111}In]-cholera toxin, at the times indicated in Fig. 2*D–F*.

Immunization and sample collection

The cynomolgus macaques were nasally immunized with 500 μg per 500 μl BoHc/A (250 μl, each nostril), on four different occasions, at 2-wk intervals. Before immunization and 7 d postimmunization, serum and nasal wash samples were collected for the determination of BoNT/A-specific Ab titers.

ELISA

BoNT/A (5 μg/ml, 100 μl) was coated onto 96-well microtiter plates overnight at 4°C. Nonspecific binding to the plates was blocked with 1% BSA, and then 2-fold serial dilutions of samples were added and incubated for 2 h at room temperature. After washing, HRP-conjugated goat anti-monkey IgG (Nordic Immunological Laboratory, Tilburg, Netherlands) or HRP-conjugated goat anti-monkey IgA (Cortex Biochem, San Leandro, CA) diluted 1:1000 were added and incubated for 2 h at RT together with 1% normal goat serum (Vector, Burlingame, CA). The reaction was finally developed with the use of the TMB Microwell Peroxidase Substrate System (XPL, Gaithersburg, MD). End-point titers were expressed as the reciprocal log2 of the last dilution, which gave an OD450 of 0.1 greater than the negative control.

PET/MRI imaging in nonhuman primates

After nasal administration of [^{18}F]-BoHc/A (34.5 MBq [18.1 μg] per 315 μl and 54.7 MBq [28.6 μg] per 500 μl) to male rhesus macaques (n = 2), each macaque's head was tilted back for 10 min and then scanned in an upright position after anesthesia. PET scans were conducted for 345 min with frames of 25 × 3 min, followed by 27 × 10 min, with the use of a high-resolution animal PET scanner (SHR-7700; Hamamatsu Photonics, Shizuoka, Japan) (22). An MRI scan was obtained by using a MAGNETOM Allegra (3T; Siemens, Munich, Germany) to identify cerebrum regions. After PET imaging, the [^{18}F] radioactivity within each dissected organ of the macaque, including brain and OB, was directly measured by a gamma counter (1480 Wizard).

Data analysis of images

PET data were analyzed by means of the PMOD software package (PMOD Technologies, Zurich, Switzerland). Each PET image was superimposed on the corresponding MRI or CT data to identify the volume of interest. SUVs were calculated from the level of radioactivity in the volume of interest. PET images were presented as a maximum intensity projection (MIP) image. TACs of PET images were based on SUVs.

Results

In vivo quantitative imaging and whole-body imaging of nasally administered [^{18}F]-BoHc/A in mice

[^{18}F]-BoHc/A was synthesized after expression of recombinant BoHc/A in *Escherichia coli* and purification by chromatography (Supplemental Figs. 1 and 2). Mice were nasally administered 0.9 MBq per 20 μl [^{18}F]-BoHc/A (10 μl per nostril) and were then subjected to anesthesia after 5 min to allow immediate analysis by PET together with CT (PET/CT) or by means of a PPIS. The MIP images of PET data, which were obtained from 10 min to 10 h after nasal administration, were coregistered with a CT surface rendering image, and sites of [^{18}F]-BoHc/A accumulation were identified by image fusion analysis (Fig. 1*A*). PET data obtained 50–60 min after nasal administration of [^{18}F]-BoHc/A were also visualized as an MIP image coregistered with a CT image to produce a three-dimensional view of a mouse (Supplemental Video 1). Quantitative TACs of [^{18}F]-BoHc/A from the PET data showed that the nasal cavity and urinary bladder were major sites of accumulation of radioactive material after 10 h, whereas the throat, stomach, and intestine were temporary sites of accumulation of radioactive material (Fig. 1*B*). The whole-body imaging by PPIS (Supplemental Video 2 and Fig. 3) showed dynamic imaging of [^{18}F]-BoHc/A in the nasal cavity, throat, stomach, intestine, and urinary bladder in mice from 10 min to 10 h after nasal administration. [^{18}F]-BoHc/A was detected in the nasal cavity throughout the entire examination period.

Tissue distribution of nasally administered [^{18}F]-BoHc/A analyzed by direct tissue counting in mice

When the tissue distribution of [^{18}F]-BoHc/A was quantified by direct counting of radioactivity (Fig. 2*A*), [^{18}F]-BoHc/A was found to be preferentially located in urine and in the nasal cavity and, in decreasing order of abundance, in the esophagus, stomach, intestine, feces, nasopharynx-associated lymphoid tissue, and kidney. These data are consistent with the quantitative TACs of [^{18}F]-

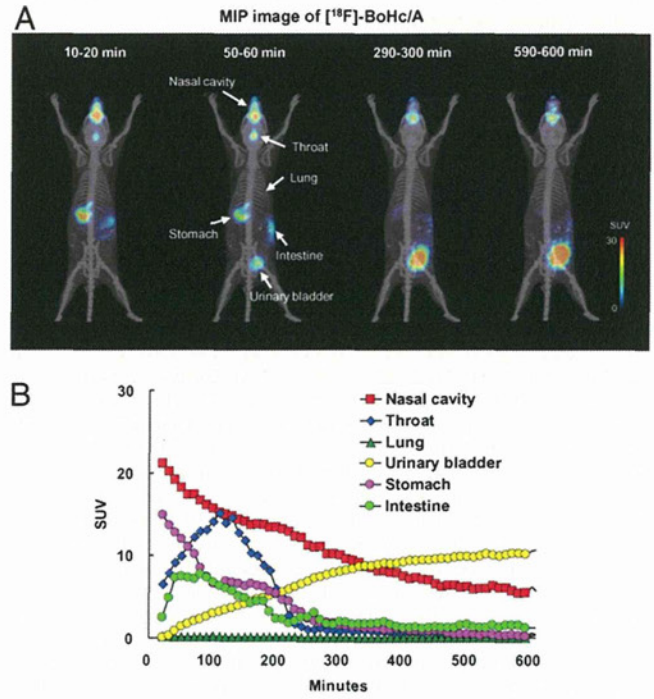

FIGURE 1. PET/CT imaging and TACs for nasal administration of [^{18}F]-BoHc/A in mice. After nasal administration of [^{18}F]-BoHc/A, the mouse was placed in a small animal PET system and the whole body was scanned for 10 h. A CT scan was then performed to identify organs and tissues. *A*, PET/CT scanning obtained at the indicated time is shown as the MIP images for the coronal planes in the mouse. *B*, TACs of nasal cavity, throat, lung, stomach, intestine, and urinary bladder at 10 h after administration of [^{18}F]-BoHc/A are presented. It was noted that accumulation of [^{18}F]-BoHc/A was not found in lung after nasal administration.

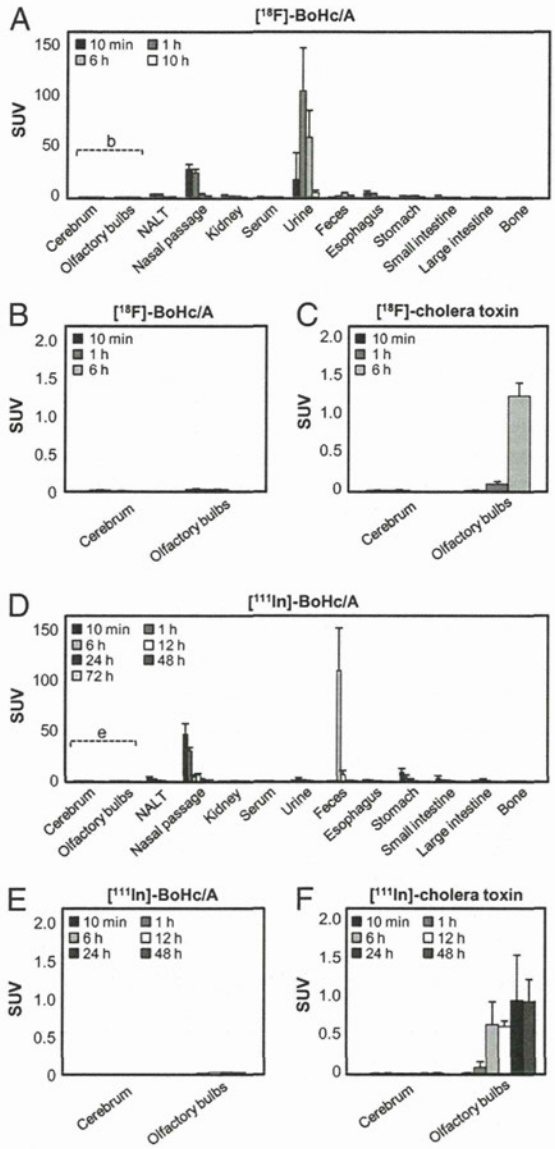

FIGURE 2. SUVs of tissues after nasal administration of [^{18}F]-BoHc/A or [^{111}In]-BoHc/A in mice. *A*, After nasal administration of [^{18}F]-BoHc/A, the isotope activity in each mouse tissue at the indicated time (n = 3 per time point) was measured directly and displayed as SUV. *B*, To further check whether there is an accumulation of [^{18}F]-BoHc/A in the CNS, we enlarged the SUV scale for cerebrum and OBs to focus on levels near the detection limit in the experiment above. *C*, Nasal administration of [^{18}F]-cholera toxin was used as a positive control; this toxin accumulated in the OBs but not the cerebrum at 6 h on the enlarged SUV scale (n = 3 per time point). *D*, After nasal administration of [^{111}In]-BoHc/A, the isotope activity of each mouse tissues at the indicated time (n = 3 per time point) was measured directly and displayed as SUV. *E*, To further check whether there is an accumulation of [^{111}In]-BoHc/A in CNS in the experiment above, we enlarged the SUV scale for cerebrum and OBs. *F*, Nasal administration of [^{111}In]-cholera toxin was used as a positive control; this toxin accumulated in the OBs but not cerebrum from 6 h on the enlarged SUV scale (n = 3 per time point). Error bar shows SD. NALT, nasopharynx-associated lymphoid tissue.

BoHc/A in mice obtained by PET/CT imaging (Fig. 1*B*). Furthermore, we could not detect [^{18}F]-BoHc/A in the CNS, including the OB and cerebrum (Fig. 2*B*). The accumulated [^{18}F]-BoHc/A in the cerebrum and OB were lower than 0.01 and 0.04 SUV within the 6-h period after nasal administration of 0.90 MBq per 20 μl [^{18}F]-BoHc/A to each mouse, respectively. In contrast, the positive control [^{18}F]-cholera toxin was detected in the OB at 6 h after nasal administration of 0.56 MBq per 20 μl [^{18}F]-cholera toxin (Fig. 2*C*). When the radioactive samples extracted from nasal cavity and esophagus were further examined by size-exclusion chromatography on prepacked disposable (PD-10) columns (GE Healthcare UK, Buckinghamshire, U.K.), [^{18}F]-BoHc/A was found in the high m.w. fractions. The radioactivity detected in samples from the digestive tract, which included stomach, small intestine, and feces, was present in both high and low m.w. forms, whereas that in the urine sample was present only in low m.w. forms (Fig. 3*A*).

Analysis of the longevity of the nasal vaccine in mouse tissues by using [^{111}In]-BoHc/A

We used the traditional [^{111}In]-radiolabel method to examine the persistence of the nasal BoHc/A vaccine in mouse tissues. Because the half-life of [^{111}In] is 67.3 h, we counted the radioactivity in

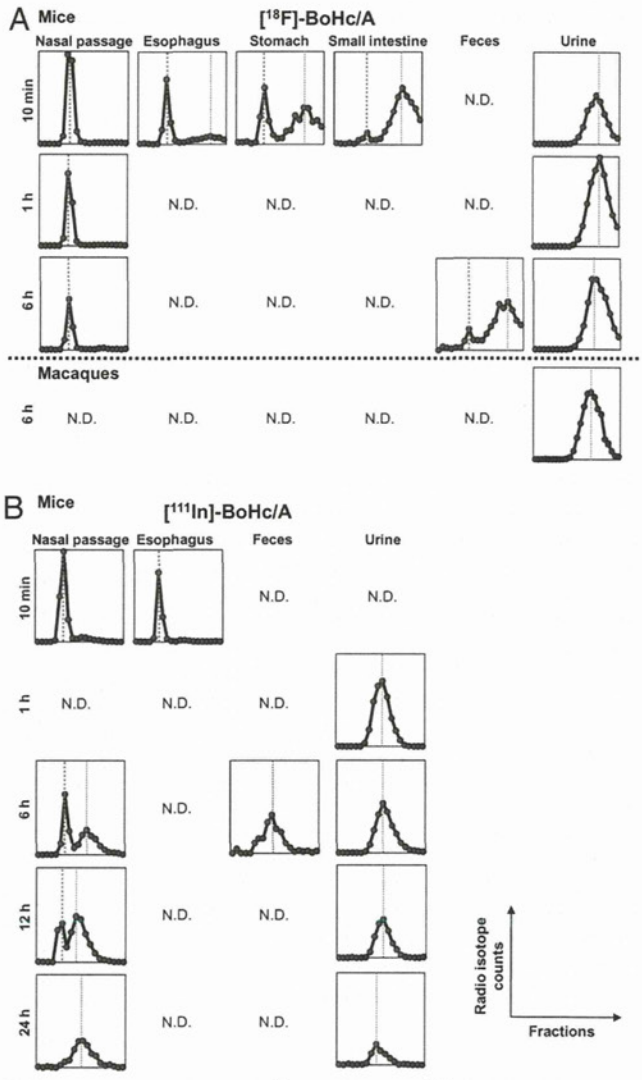

FIGURE 3. Degradation of [^{18}F]-BoHc/A or [^{111}In]-BoHc/A in tissues after nasal administration. *A*, The supernatants of homogenized tissues and feces, and urine at indicated time from mice or macaques taken after nasal administration of [^{18}F]-BoHc/A were loaded onto a prepacked PD-10 column containing Sephadex G-10 (GE Healthcare) and fractionated; the [^{18}F] radioactivity was then counted directly by using a gamma counter. *B*, The supernatants of homogenized tissues and feces, and urine at indicated time from mice or macaques taken after nasal administration of [^{111}In]-BoHc/A were fractionated with PD-10 column, and the [^{111}In] radioactivity was then counted directly by using a gamma counter. Tissue samples with low radioactivity were not determined (N.D.).